ISSN 1674-1056
http://cpb.iphy.ac.cn
http://iopscience.iop.org/cpb
中国物理 B
Chinese Physics
中国物理
Chinese Physics B

Modeling electric field of power metal-oxide-semiconductor field-effect transistor with dielectric trench based on Schwarz-Christoffel transformation

Zhi-Gang Wang(汪志刚), Tao Liao(廖涛), Ya-Nan Wang(王亚南)

Citation: Chin. Phys. B . 2019, 28(5): 058503. **doi:** 10.1088/1674-1056/28/5/058503
Journal homepage: http://cpb.iphy.ac.cn; http://iopscience.iop.org/cpb

What follows is a list of articles you may be interested in

An analytical model for the vertical electric field distribution and optimization of high voltage REBULF LDMOS

Hu Xia-Rong, Lü Rui
Chin. Phys. B . 2014, 23(12): 128501. **doi:** 10.1088/1674-1056/23/12/128501

Low on-resistance high-voltage lateral double-diffused metal oxide semiconductor with a buried improved super-junction layer

Wu Wei, Zhang Bo, Luo Xiao-Rong, Fang Jian, Li Zhao-Ji
Chin. Phys. B . 2014, 23(3): 038503. **doi:** 10.1088/1674-1056/23/3/038503

High voltage super-junction lateral double diffused metal-oxide semiconductor with partial lightly doped pillar

Wu Wei, Zhang Bo, Fang Jian, Luo Xiao-Rong, Li Zhao-Ji
Chin. Phys. B . 2013, 22(6): 068501. **doi:** 10.1088/1674-1056/22/6/068501

Analytical models of lateral power devices with arbitrary vertical doping profiles in drift region

Hua Ting-Ting, Guo Yu-Feng, Yu Ying, Gene Sheu, Jian Tong, Yao Jia-Fei
Chin. Phys. B . 2013, 22(5): 058501. **doi:** 10.1088/1674-1056/22/5/058501

High-field-induced electron detrapping in An AlGaN/GaN high electron mobility transistor

Fu Li-Hua, Lu Hai, Chen Dun-Jun, Zhang Rongm, Zheng You-Dou, Wei Ke, Liu Xin-Yu
Chin. Phys. B . 2012, 21(10): 108503. **doi:** 10.1088/1674-1056/21/10/108503

Modeling electric field of power metal-oxide-semiconductor field-effect transistor with dielectric trench based on Schwarz–Christoffel transformation*

Zhi-Gang Wang(汪志刚)†, Tao Liao(廖涛), and Ya-Nan Wang(王亚南)

School of Information Science and Technology, Southwest Jiao Tong University, Chengdu 611756, *China*

(Received 19 December 2018; revised manuscript received 6 March 2019; published online 8 April 2019)

A power metal-oxide-semiconductor field-effect transistor (MOSFET) with dielectric trench is investigated to enhance the reversed blocking capability. The dielectric trench with a low permittivity to reduce the electric field at reversed blocking state has been studied. To analyze the electric field, the drift region is segmented into four regions, where the conformal mapping method based on Schwarz–Christoffel transformation has been applied. According to the analysis, the improvement in the electric field for using the low permittivity trench is mainly due to the two electric field peaks generated in the drift region around this dielectric trench. The analytical results of the electric field and the potential models are in good agreement with the simulation results.

Keywords: conformal mapping, Schwarz–Christoffel transformation, electric field, trench metal-oxide-semiconductor field-effect transistor (MOSFET), breakdown voltage

PACS: 85.30.De, 77.30.df, 51.50.+v **DOI:** 10.1088/1674-1056/28/5/058503

1. Introduction

Lateral double-diffused metal-oxide-semiconductor (LDMOS) devices that use a dielectric trench in the drift region have been investigated for power applications owing to the small device cell with a high breakdown voltage (BV).[1–6] The dielectric trench in the drift region of LDMOS devices is adopted as an effective technique to enhance breakdown voltage and reduce specific on-resistance $R_{on,sp}$.[7–11] State-of-the-art LDMOS devices obtained by the dielectric trench to sustain a high reversed voltage have been reported.[12–17] In these devices, breakdown occurs in the drift region for the crowded electric field.[18,19] Several analytical models for the conventional LDMOS devices have been reported to approximate the surface electric field.[20–27] For the LDMOS devices with dielectric trench, the electric field and BV in an irregular drift region are difficult to obtain.[28–30]

In this paper, a lateral trench metal-oxide-semiconductor field-effect transistor (MOSFET) on silicon-on-insulator (SOI) with low permittivity dielectric is studied. It is important to note that in the drift region around the dielectric trench, the potential contours are not distributed uniformly as in the conventional LDMOS devices. In this U-shaped drift region, a Schwarz–Christoffel transformation is applied to transform the U-shaped drift region to the parallel region to simplify the calculation of the electric field.[31] The analytical model of the electric field and BV can be analytically calculated and verified by simulation.

2. Model of trench MOSFET

As shown in Fig. 1, there is a power MOSFET with a dielectric trench sandwiched by the N-pillar on the right and P-pillar on the left on SOI. The trench is filled with the low-k dielectric in the upper portion and with SiO_2 in the lower section. The P-pillar is located on the left of the dielectric trench and the N-pillar is located on the right of the dielectric trench, as shown in Fig. 1. At the top of the trench MOSFET, from left to right are the trench gate, source, dielectric trench, and drain. At the bottom of the trench MOSFET, buried-oxide layer (BOX) is sitting on the P-substrate and is connected to the substrate electrode. Around the dielectric trench, the drift region contains four parts: regions I, II, III, and IV. The N drift region and P-pillar constitute region I, and the N-pillar and N drift region constitute region IV. Two insulator materials with a low-k dielectric and silicon dioxide SiO_2 have been used for the trench dielectric. Since a reversed bias is applied between the source and drain across the dielectric trench, the whole drift region must sustain this applied bias as the dielectric trench. When breakdown occurs, the peak of the electric field is generated along the path A–O_1–B–C–O_2–D in the silicon drift region. Based on the avalanche breakdown theory, the integration of the electric field along this path is equal to the breakdown voltage, which could be obtained by solving Poisson's equation. Thus, the U-shaped drift region is generally divided into four parts—i.e., regions I, II, III, and IV—to calculate the analytical electric field distribution.

*Project supported by the National Natural Science Foundation of China (Grant No. 61404110) and the National Higher-education Institution General Research and Development Project, China (Grant No. 2682014CX097).

†Corresponding author. E-mail: zhigangwang@swjtu.edu.cn

© 2019 Chinese Physical Society and IOP Publishing Ltd

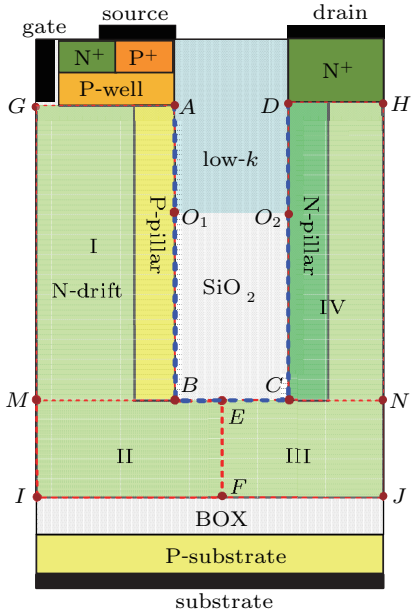


Fig. 1. Schematic diagram of the power MOSFET device with a dielectric trench.

2.1. Modeling regions II & III

The Schwarz–Christoffel maps are utilized for regions II and III, as shown in Fig. 1. The rectangle polygons with an asymmetric geometry as shown in the z-plane of Figs. 2(a) and 3(a) could be transferred from an asymmetric plane into a mirror-symmetric geometry; i.e., the semi-parallel plate structures as shown in the τ-plane of Figs. 2(c) and 3(c). These contain two steps for conformal mapping: (i) is the Schwarz–Christoffel transformation and (ii) is inverted Schwarz–Christoffel transformation.

(i) In the first step, the conformal maps from the original z-plane of region II as shown in Fig. 2(a) and region III as shown in Fig. 3(a) are transformed into the upper half-plane (ω-plane) by the Schwarz–Christoffel transformation. For this transformation, the bounded polygons with vertices *I–F–E–B–M* in region II of Fig. 2 and *N–C–E–F–J* in region III of Fig. 3, are numbered counter-clockwise to obtain the interior angles of the corresponding vertices. These interior angles of these vertices *I–F–E–B–M* are π, $\pi/2$, $\pi/2$, π, and 2π, and of *N–C–E–F–J* are 2π, π, $\pi/2$, $\pi/2$, and π, respectively.

(ii) In the second transformation, the upper region above the line *I–F–E–B–M* in the ω-plane is transformed into semi-rectangular region in the τ-plane, as shown in Fig. 2(c). The interior angles of *I–F–E–B–M* based on the Schwarz–Christoffel (SC) transformation from the τ-plane to ω-plane as shown in Fig. 2 are π, $\pi/2$, π, $\pi/2$, and 2π, respectively. Similarly, in Fig. 3, the interior angles are π at J, $\pi/2$ at F, π at E, $\pi/2$ at C, and 2π at N. The inverted Schwarz–Christoffel transformation is used to map the ω-plane into τ-plane. For the Schwarz–Christoffel transformation, the reflection pattern is listed in Table 1.

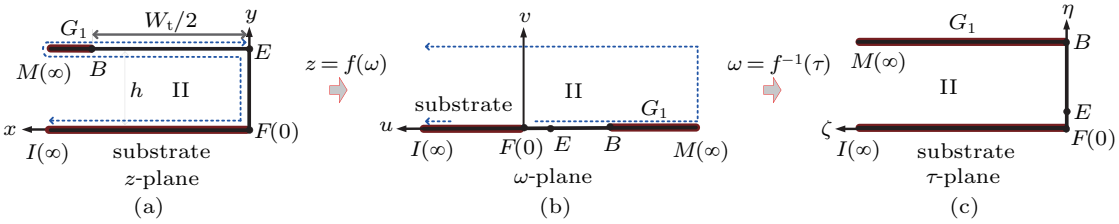


Fig. 2. Schwarz–Christoffel mapping: (a) region II in the original z-plane; (b) the structure after a conformal transformation into the ω-plane; (c) the corresponding structure after the second conformal transformation into the τ-plane.

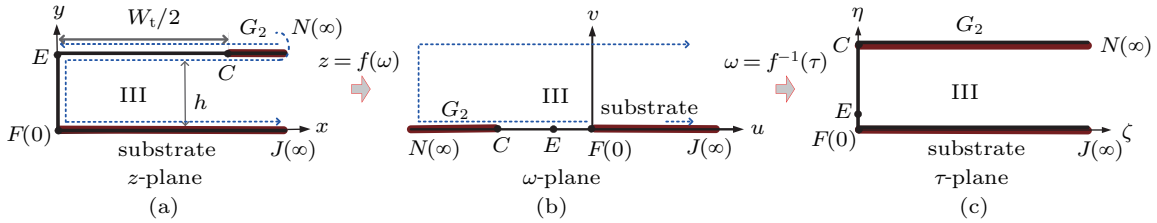


Fig. 3. Schwarz–Christoffel mapping: (a) region III in the original z-plane; (b) the structure after a conformal transformation into the ω-plane; (c) the corresponding structure after the second conformal transformation into the τ-plane.

Therefore, the Schwarz–Christoffel transformation for a half-plane from Fig. 2(a) to Fig. 2(b) is

$$z = \alpha_1 + \alpha_2 \int \omega^{-1/2}(\omega+1)^{-1/2}\mathrm{d}\omega. \tag{1}$$

Substituting the coordinates of points F and E into Eq. (1), one obtains that $\alpha_1 = 0$ and $\alpha_2 = h/\pi$. Then, the transfer function from the z-plane to ω-plane is rewritten as

$$x + y\mathrm{i} = \frac{2h}{\pi}\mathrm{arcsinh}\left(\omega^{1/2}\right). \tag{2}$$

Transforming from Fig. 2(b) to Fig. 2(c), the Schwarz–Christoffel formula is[32]

$$\frac{\mathrm{d}\tau}{\mathrm{d}\omega} = \omega^{-1/2}\left(\omega + \cosh\left(\frac{\pi W_\mathrm{t}}{4h}\right)^2\right)^{-1/2}, \tag{3}$$

where W_t is the width of the trench. Based on the in-

verse Schwarz–Christoffel transformation, from the upper half-plane ω-plane to the semi-strip τ-plane, the conformal mapping formula $\omega = f(\tau)$ is rewritten as

$$u + v\mathrm{i} = \frac{1}{16}(\mathrm{e}^{-\frac{\pi W_\mathrm{t}}{4h}} + \mathrm{e}^{\frac{\pi W_\mathrm{t}}{4h}})^2(-\mathrm{e}^{-\frac{\tau}{2}} + \mathrm{e}^{\frac{\tau}{2}})^2. \quad (4)$$

The corresponding transformation of Fig. 3 can be obtained as Eqs. (2) and (4). The vertex points are listed in Table 1.

In regions II and III of the original plane, Poisson's equation could be written as

$$\frac{\partial^2 \psi_k(x,y)}{\partial x^2} + \frac{\partial^2 \psi_k(x,y)}{\partial y^2} = -\frac{\rho_k}{\varepsilon_\mathrm{s}}, \quad k = 2,3, \quad (5)$$

where ε_s is the permittivity of silicon, and the index $k = 2$ represents region II and $k = 3$ for region III. In the τ-plane, the potential solution $\psi_k(u,v)$ in Eq. (5) could be approximated by a parabolic function as[33]

$$\psi_k(\zeta,\eta) = \gamma_k(\zeta) + a_{k1}(\zeta)\eta + a_{k2}(\zeta)\eta^2, \quad k = 2,3, \quad (6)$$

where $\psi_{k=2}(\zeta,\eta)$ represents the potential distribution in region II and $\psi_{k=3}(\zeta,\eta)$ represents the potential distribution in region III. At $\eta = 0$ as shown in Figs. 2(c) and 3(c), $\psi_k(\zeta,0) = \gamma_k(\zeta)$. In the τ-plane, the potential in the η-direction is assumed to be parabolic distribution. Assuming $\eta = 0$, the Poisson's equation in the τ-plane transformed from Eq. (5) of the original plane (z-plane) is simplified as

$$\frac{\mathrm{d}^2\gamma_k(\zeta)}{\mathrm{d}\zeta^2} + 2a_{k2}(\zeta) = -\frac{\rho_\tau}{\varepsilon}\bigg|_{\eta=0}, \quad k = 2,3, \quad (7)$$

where the charge concentration of ρ_τ in the τ-plane is $\rho_\tau = \rho_k\left|\frac{\mathrm{d}z}{\mathrm{d}\tau}\right|^2$.[32] In regions II and III in the τ-plane as shown in Figs. 2 and 3, the corresponding boundary and continuity conditions could also be found for Eq. (6).

At $\zeta = 0$ and $\eta = \pi$, the potential boundary condition in region II of τ-plane is $\psi_2(0,\pi) = V_1$. After conformal mapping, it is rewritten as

$$\frac{\partial \psi_3(\zeta,\pi)}{\partial \eta} = a_{21}(\zeta) + 2\pi a_{22}(\zeta) = E_2. \quad (8)$$

At $\zeta = 0$ and $\eta = \pi$, the potential boundary condition in region III of τ-plane is $\psi_3(0,\pi) = V_2$. In the τ-plane, the boundary condition is

$$\frac{\partial \psi_4(\zeta,\pi)}{\partial \eta} = a_{31}(\zeta) + 2\pi a_{32}(\zeta) = E_3, \quad (9)$$

where E_2 and E_3 are the electric fields of points B and C, respectively.

Table 1. Coordinates of the corresponding points on the three-plane surface-field-based discrete core model.

Point	z-plane	ω-plane	τ-plane
B	$W_\mathrm{t}/2 + \mathrm{i}h$	$-1/2 - (\mathrm{e}^{\frac{-\pi W_\mathrm{t}}{2h}} + \mathrm{e}^{\frac{\pi W_\mathrm{t}}{2h}})/4$	$\mathrm{i}\pi$
C	$W_\mathrm{t}/2 + \mathrm{i}h$	$-1/2 - (\mathrm{e}^{\frac{-\pi W_\mathrm{t}}{2h}} + \mathrm{e}^{\frac{\pi W_\mathrm{t}}{2h}})/4$	$\mathrm{i}\pi$
E	$\mathrm{i}h$	-1	$-\mathrm{i}\cdot 2\mathrm{arcsinh}(\mathrm{sech}(\pi W_\mathrm{t}/4\,h))$
F	0	0	0
I	∞	∞	∞
J	∞	∞	∞
M	$\infty + \mathrm{i}h$	∞	$\infty + \mathrm{i}\pi$
N	$\infty + \mathrm{i}h$	∞	$\infty + \mathrm{i}\pi$

At the B–E–F and C–E–F lines of regions II and III in the τ-plane, the continuity condition is simplified into

$$\frac{\partial \psi_k\left(\zeta, -2\mathrm{i}\cdot\mathrm{arcsinh}\left(\frac{2\mathrm{e}^{\frac{\pi W_\mathrm{t}}{4h}}}{1+\mathrm{e}^{\frac{\pi W_\mathrm{t}}{2h}}}\right)\right)}{\partial \zeta} = 0. \quad (10)$$

Based on the continuity boundary condition of the electric displacement at the interface of the drift region and BOX, one obtains

$$a_{k1}(\zeta) = \frac{\partial \psi_k(\zeta,0)}{\partial v} = \frac{\varepsilon_\mathrm{ox}}{\varepsilon_{sk}}\frac{\gamma_k(\zeta)}{W_\mathrm{BOX}}, \quad (11)$$

$$a_{k2}(\zeta) = \frac{\lambda_k}{2} - \frac{\varepsilon_\mathrm{ox}}{2\pi\varepsilon_{si}W_\mathrm{BOX}}\gamma_k(\zeta), \quad (12)$$

where $\lambda_2 = E_2/\pi$, and $\lambda_3 = E_3/\pi$.

Combining Eqs. (8)–(12) (boundary condition of regions II and III), the $\gamma_k(\zeta)$ in Eq. (6) for the general solution is expressed as

$$\gamma_k(\zeta) = C_k\exp(\zeta/T) + C_k'\exp(-\zeta/T) + \beta_1\zeta^2 + \beta_2, \quad (13)$$

where

$$T = \sqrt{\frac{\pi\varepsilon_\mathrm{s}W_\mathrm{BOX}}{\varepsilon_\mathrm{ox}}},$$

$$\beta_1 = \frac{qN_\mathrm{d}h^2T^2(1-\cosh(\pi W_\mathrm{t}/2h))}{32\pi^2\varepsilon_\mathrm{s}},$$

$$\beta_2 = T^2\left[\frac{qN_\mathrm{d}h^2(1+\cosh(\pi W_\mathrm{t}/2h))}{2\pi^2\varepsilon_\mathrm{s}} + \frac{E_k}{\pi} + 2\beta_1\right],$$

C_k and C_k' are constants which could be obtained by the boundary condition and the continuity condition. $C_{k=2}$ in region II and $C_{k=3}$ in region III have been obtained as

$$C_2 = \frac{2W_{\rm BOX}\varepsilon_{\rm s}(-W_{\rm BOX}\varepsilon_{\rm s}E_{x2} - \pi\varepsilon_{\rm ox}E_{x2} + \varepsilon_{\rm ox}V_1)}{\varepsilon_{\rm ox}(2W_{\rm BOX}\varepsilon_{\rm s} + \pi\varepsilon_{\rm ox})} + \frac{qN_{\rm d}W_{\rm BOX}h^2[-8\varepsilon_{\rm ox}(1+\cosh(\frac{\pi W_{\rm t}}{2h})) - \pi\varepsilon_{\rm s}W_{\rm BOX}(1-\cosh(\frac{\pi W_{\rm t}}{h}))}{16\pi\varepsilon_{\rm ox}^2}, \quad (14)$$

$$C_3 = \frac{2W_{\rm BOX}\varepsilon_{\rm s}(-W_{\rm BOX}\varepsilon_{\rm s}E_{x3} - \pi\varepsilon_{\rm ox}E_{x3} + \varepsilon_{\rm ox}V_2)}{\varepsilon_{\rm ox}(2W_{\rm BOX}\varepsilon_{\rm s} + \pi\varepsilon_{\rm ox})} + \frac{qN_{\rm d}W_{\rm BOX}h^2[-8\varepsilon_{\rm ox}(1+\cosh(\frac{\pi W_{\rm t}}{2h})) - \pi\varepsilon_{\rm s}W_{\rm BOX}(1-\cosh(\frac{\pi W_{\rm t}}{h}))}{16\pi\varepsilon_{\rm ox}^2}, \quad (15)$$

$$C_2' = C_3' = 0, \quad (16)$$

$$E_{kx} = -\frac{\partial\psi_k(x,y)}{\partial x} = -\left|\frac{{\rm d}\tau}{{\rm d}z}\right|\frac{\partial\psi_k(\zeta,\eta)}{\partial\zeta}, \quad (17)$$

$$E_{ky} = -\frac{\partial\psi_k(x,y)}{\partial y} = -\left|\frac{{\rm d}\tau}{{\rm d}z}\right|\frac{\partial\psi_k(\zeta,\eta)}{\partial\zeta}. \quad (18)$$

2.2. Modeling regions I & IV

In regions I and IV, as shown in Fig. 4, Poisson's equation could be written as

$$\frac{\partial^2\psi_k(x,y)}{\partial x^2} + \frac{\partial^2\psi_k(x,y)}{\partial y^2} = -\frac{\rho_k}{\varepsilon_{\rm s}}, \quad k = 1,4, \quad (19)$$

where ρ_k is the charge concentration, and the index k of 1 and 4 represents regions I and IV, respectively.

Boundary conditions in regions I and IV are

(A) $\psi_1(x,L/2) = 0$ and $\psi_1(x,-L/2) = V_1$, since the voltage V_1 at the bottom of region I could be regarded as a continuity condition of region II.

(B) $\psi_4(x,L/2) = V_{\rm d}$ and $\psi_4(x,-L/2) = V_2$, since the voltage V_2 at the bottom of region IV could be regarded as a continuity condition of region III. The $V_{\rm d}$ indicates the applied bias between the drain and the source.

(C) For $0 < y < L/2$, at the interface of the P-pillar and the trench, the displacement continuity condition along the interface of the pillar and the trench in regions I and IV could be obtained as $\varepsilon_{\rm s}\partial\psi_k/\partial x = \varepsilon_{I1}\partial\psi_k/\partial x$, where ε_{I1} is the permittivity of the dielectric material in trench. The continuity of the electric displacement at the interface of the P-pillar and the trench is another important condition.

(D) For $-L/2 < y < 0$, the continuity condition at the interface of the P-pillar and BOX is $\varepsilon_{\rm s}\partial\psi_k/\partial x = \varepsilon_{I2}\partial\psi_k/\partial x$, where ε_{I2} is the permittivity of the dielectric material in trench.

(E) At $y = 0$, the potential and the electric field are also shown as

$$\psi_k(x,y)|_{x=0^-} = \psi_k(x,y)|_{x=0^+}, \quad (20)$$

$$\frac{\partial\psi_3(x,y)}{\partial x}|_{x=0^-} = \frac{\partial\psi_3(x,y)}{\partial x}|_{x=0^+}, \quad (21)$$

$$\frac{\partial\psi_4(x,y)}{\partial x}|_{x=0^-} = \frac{\partial\psi_4(x,y)}{\partial x}|_{x=0^+}. \quad (22)$$

Since the reversed bias is much larger than the built-in potential, the built-in potential is neglected in the model for calculating the electric field. In order to find the solution of the Poisson's equation, the equivalent potential is assumed at $y = 0$ and $y = -L/2$ as: $\psi_1|_{y=0} = V_0$, $\psi_1|_{y=-L/2} = V_1$, $\psi_4|_{y=0} = V_3$, and $\psi_4|_{y=-L/2} = V_2$.

The solution of the Poisson's equation could be superposed by two parts as

$$\psi_k(x,y) = \xi_k(x,y) + \phi_k(x,y). \quad (23)$$

The first term $\xi_k(x,y)$ is the potential, yielded by the applied bias and the depletion charges, which could be approximated by a quadratic function. The second term $\phi_k(x,y)$ satisfies the Laplace's equation.

(F) In region I, the boundary conditions are $\xi_1(0) = V_0$ and $\xi_1(-L/2) = V_1$, and in region IV, the boundary conditions are $\xi_4(-L/2) = V_2$ and $\xi_4(L/2) = V_{\rm d}$.

$$\begin{aligned}
&\frac{\partial^2\xi_k(y)}{\partial y^2} = -\frac{\rho_k}{\varepsilon_{\rm s}},\\
&\xi_1(0) = V_0, \quad \xi_4(0) = V_3,\\
&\xi_1(L/2) = 0, \quad \xi_4(L/2) = V_{\rm d},\\
&\xi_1(-L/2) = V_1, \quad \xi_4(-L/2) = V_2,
\end{aligned} \quad (24)$$

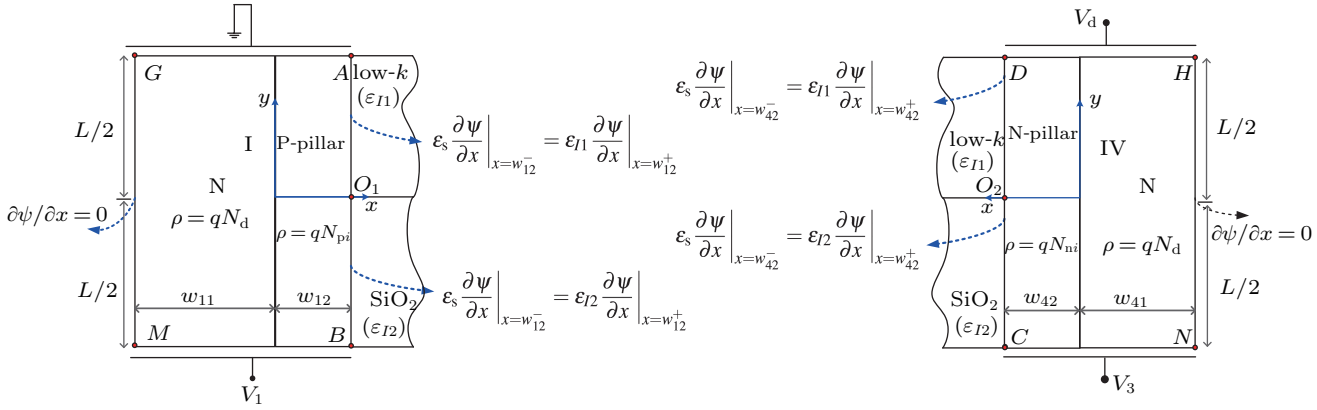


Fig. 4. Simplification of the structure and the boundary condition: (a) region I and (b) region IV.

where

$$\rho_1 = \begin{cases} qN_{\rm d}, & -w_{11} < x < 0, \\ -qN_{\rm pk}, & 0 < x < w_{12}, \end{cases}$$
$$\rho_2 = \begin{cases} qN_{\rm d}, & -w_{41} < x < 0, \\ qN_{\rm nk}, & 0 < x < w_{42}. \end{cases}$$

Substituting the boundary conditions into the Poisson's equation, one obtains

$$\xi_1(y) = \begin{cases} -\dfrac{\rho_{1l}}{2\varepsilon_{\rm s}}y^2 + \dfrac{L^2\rho_1 - 8V_0\varepsilon_{\rm s}}{4\varepsilon_{\rm s}L}y + V_0, \\ 0 < y < L/2, \\ -\dfrac{\rho_1}{2\varepsilon_{\rm s}}y^2 - \dfrac{L^2\rho_1 - 8V_0\varepsilon_{\rm s} + 8V_1\varepsilon_{\rm s}}{4\varepsilon_{\rm s}L}y + V_0, \\ -L/2 < y < 0, \end{cases} \tag{25}$$

$$\xi_4(y) = \begin{cases} -\dfrac{\rho_2}{2\varepsilon_{\rm s}}y^2 + \dfrac{L^2\rho_1 - 8V_3\varepsilon_{\rm s} + 8V_{\rm d}\varepsilon_{\rm s}}{4\varepsilon_{\rm s}L}y + V_3, \\ 0 < y < L/2, \\ -\dfrac{\rho_2}{2\varepsilon_{\rm s}}y^2 - \dfrac{L^2\rho_i + 8V_2\varepsilon_{\rm s} - 8V_3\varepsilon_{\rm s}}{4\varepsilon_{\rm s}L}y + V_3, \\ -L/2 < y < 0, \end{cases} \tag{26}$$

$$V_0 = \frac{\varepsilon_{\rm ox}B_2 + (4n^2\pi^2\varepsilon_{\rm s}\varepsilon_k V_{\rm d} + +2L^2\varepsilon_k\rho_1)[1-\cos(n\pi)]}{8n^2\pi^2\varepsilon_{\rm s}} + \frac{A_2A_3(A_1+B_1)L\tanh(K_nw_{11})}{4n^2\pi^2\varepsilon_{\rm s}A_1B_1}, \tag{27}$$

$$V_0' = \frac{\varepsilon_{\rm ox}B_2 + (4n^2\pi^2\varepsilon_{\rm s}\varepsilon_k V_{\rm d} + +2L^2\varepsilon_k\rho_2)[1-\cos(n\pi)]}{8n^2\pi^2\varepsilon_{\rm s}} + \frac{A_2A_3(A_1+{\rm B}_1)L\tanh(K_nw_{21})}{4n^2\pi^2\varepsilon_{\rm s}A_1B_1}, \tag{28}$$

$$\frac{\partial^2\phi_k(x,y)}{\partial x^2} + \frac{\partial^2\phi_k(x,y)}{\partial y^2} = 0,$$
$$\phi_k(0) = 0, \quad \phi_k(L/2) = 0, \quad \phi_k(-L/2) = 0, \tag{29}$$

$$\phi_k(x,y) = \sum_{n=1}^{\infty}[D_k\cosh(K_nx) + D_k'\sinh(K_nx)]\sin(K_ny), \tag{30}$$

$$K_n = \frac{2n\pi}{L}. \tag{31}$$

To optimize BV at $x = w_{k1}$, the equipotential lines can be assumed to distribute in symmetry at the drift region for the optimized BVs. Thus, the potential contours are approximately perpendicular to the hetero-interface of the dielectric trench and the drift region in the y-direction. From this effect, it should be noted that $\frac{\partial\psi_k}{\partial x}\big|_{x=w_{k1}} = 0$ is the boundary condition at $x = w_{k1}$.

At $y = 0$, the potential and electric field are also obtained as

$$\psi_k(x,y)|_{x=0^-} = \psi_k(x,y)|_{x=0^+}, \tag{32}$$
$$\left.\frac{\partial\psi_k(x,y)}{\partial x}\right|_{x=0^-} = \left.\frac{\partial\psi_k(x,y)}{\partial x}\right|_{x=0^+}. \tag{33}$$

For $0 < y < L/2$, at the interface of the P-pillar and the trench, the displacement continuity condition could be obtained as

$$\varepsilon_{\rm s}E_{\rm si} = \varepsilon_kE_k, \tag{34}$$

where ε_k is the permittivity of the low-k dielectric material. The maximum BV of the trench MOSFET device is generally obtained at symmetric distribution of potential contours in the drift region, which are always center-divided at the bottom of the dielectric trench. Therefore, the electric field along the x-direction could be yielded as

$$\frac{\partial\psi_k}{\partial x} = \frac{\varepsilon_k}{\varepsilon_{\rm s}}\frac{V_{\rm d} - 2\psi_k}{W_{\rm t}}. \tag{35}$$

By using the boundary conditions, D_k and D_k' could be obtained as

$$D_k = \frac{H_kL\varepsilon_k}{A_1}\cosh(K_nw_{k1}) - L^2\frac{A_2A_3}{A_1}(\cos(n\pi)-1)\sinh(K_nw_{k1}), \tag{36}$$

$$D_k' = -\frac{2A_2L^3\varepsilon_{\rm s}W_{\rm t}}{A_1}\left(\frac{\varepsilon_k}{\varepsilon_{\rm s}W_{\rm t}}\cosh(K_nw_{k2}) + \frac{n\pi}{L}\sin(K_nw_{k2})\right)\sinh(K_nw_{k1}) + \frac{\varepsilon_kH_k}{A_1}. \tag{37}$$

For $-L/2 < y < 0$, the continuity condition at the interface of the P-pillar and BOX is

$$\varepsilon_{\rm s}E_{\rm si} = \varepsilon_{\rm ox}E_{\rm ox}. \tag{38}$$

Hence, the electric field along the x-direction could be obtained

$$\frac{\partial\psi_k}{\partial x} = \frac{\varepsilon_{\rm ox}}{\varepsilon_{\rm s}}\frac{V_{\rm d} - 2\psi_k}{W_{\rm t}}. \tag{39}$$

Thus

$$D_k = -\frac{{\rm B}_2L\varepsilon_{\rm ox}}{{\rm B}_1}\cosh(K_nw_{k1}) + \frac{A_2A_3L^2}{{\rm B}_1}(\cos(n\pi)-1)\sinh(K_nw_{k1}), \tag{40}$$

$$D_k' = \frac{L}{{\rm B}_1}\sinh(K_nw_{k1})\left(2A_2L^2\varepsilon_{\rm ox}\cosh(K_nw_{k2}) - \varepsilon_{\rm ox}{\rm B}_2 + 2A_2L\varepsilon_{\rm s}n\pi W_{\rm t}\sin(K_nw_{k2})\right), \tag{41}$$

where

$$A_1 = 4n^3\pi^3\varepsilon_{\rm s}(L\varepsilon_k\cosh(K_n(w_{k1}+w_{k2})) + n\pi\varepsilon_{\rm s}W_{\rm t}\sinh(K_n(w_{k1}+w_{k2}))), \tag{42}$$
$$A_2 = 2(qN_{\rm d} - \rho_k), \tag{43}$$
$$A_3 = n\pi W_{\rm t}\varepsilon_{\rm s}\cosh(K_nw_{k2}) + L\varepsilon_k\sinh(K_nw_{k2}), \tag{44}$$
$$B_1 = 4n^3\pi^3\varepsilon_{\rm s}(L\varepsilon_{\rm ox}\cosh(K_n(w_{k1}+w_{k2})) + n\pi\varepsilon_{\rm s}W_{\rm t}\sinh(K_n(w_{k1}+w_{k2}))), \tag{45}$$
$$B_2 = 8n^2\pi^2\varepsilon_{\rm s}V_k\cos(n\pi) - 2A_2L(\cos(n\pi)-1), \tag{46}$$
$$H_1 = (2L^2\rho_1 + 4n^2\pi^2\varepsilon_{\rm s}V_{\rm d})(1-\cos(n\pi)) - 8n^2\pi^2\varepsilon_{\rm s}V_0, \tag{47}$$
$$H_2 = \left(2L^2\rho_2 + 4n^2\pi^2\varepsilon_{\rm s}V_{\rm d}\right)(1-\cos(n\pi)) - 8n^2\pi^2\varepsilon_{\rm s}V_3. \tag{48}$$

According to the potential distribution around the trench as given in Eqs. (25)–(28), the electric field of regions I and IV could be obtained as

$$E_{kx} = \sum_{n=1}^{\infty}[C_iK_n\sinh(K_nx) + D_iK_n\cosh(K_nx)]\sin(K_ny), \tag{49}$$

$$E_{1y}=\begin{cases}-\dfrac{\rho_1}{\varepsilon_s}y+\dfrac{L^2\rho_1-8V_0\varepsilon_s}{4\varepsilon_sL}+\sum\limits_{n=1}^{\infty}K_n[D_i\sinh(K_nx)+C_i\cosh(K_nx)]\cos(K_ny), & 0<y<L/2,\\ -\dfrac{\rho_1}{\varepsilon_s}y-\dfrac{L^2\rho_1-8V_0\varepsilon_s+8V_1\varepsilon_s}{4\varepsilon_sL}+\sum\limits_{n=1}^{\infty}K_n[D_i\sinh(K_nx)+C_i\cosh(K_nx)]\cos(K_ny), & -L/2<y<0,\end{cases} \tag{50}$$

$$E_{2y}=\begin{cases}-\dfrac{\rho_2}{\varepsilon_s}y+\dfrac{L^2\rho_2-8V_3\varepsilon_s+8V_d\varepsilon_s}{4\varepsilon_sL}+\sum\limits_{n=1}^{\infty}K_n[D_i\sinh(K_nx)+C_i\cosh(K_nx)]\cos(K_ny), & 0<y<L/2,\\ -\dfrac{\rho_2}{\varepsilon_s}y-\dfrac{L^2\rho_2+8V_2\varepsilon_s-8V_3\varepsilon_s}{4\varepsilon_sL}+\sum\limits_{n=1}^{\infty}K_n[D_i\sinh(K_nx)+C_i\cosh(K_nx)]\cos(K_ny), & -L/2<y<0.\end{cases} \tag{51}$$

The breakdown voltage could be calculated by the integration of the electric field along the path A–O_1–B–C–O_2–D. Then the optimized breakdown voltage $\mathrm{BV_{opt}}$[13] could be approximated in the polynomial terms of the structure parameters as

$$\mathrm{BV_{opt}}=\frac{5.56\times10^{-11}(1+0.023L^2)}{L}\times\left[1+(N_d^{0.96677}-0.2946N_d)W_t^{-0.178}k_r^{-0.023}\right]. \tag{52}$$

3. Results and discussion

To assess the validity of the analytical model, three types of the trench MOSFETs have been studied. Figure 5(a) shows the trench MOSFET1 with the low-k material at the top and SiO_2 at the bottom of the trench. Figure 5(b) shows the trench MOSFET2 with the trench filled with SiO_2. A trench MOSFET3 with the low-k material at the top and SiO_2 at the bottom and without N- and P-pillars is shown in Fig. 5(c). The corresponding parameters of the three types of MOSFETs are listed in Table 2.

When the reversed bias applied to the drain-to-source approaches the breakdown voltage, the drift region of the three types of trench MOSFETs is fully depleted. The potential contours pass through the dielectric trench between the source and the drain. The peaks of the electric field distribution in the silicon drift region exist around the dielectric trench along A–B–C–D as shown in Fig. 5, with the maximum electric field determining the onset of the avalanche breakdown. Figure 6 shows the electric fields along the A–B–C–D line for the three trench MOSFETs. For trench MOSFET1, MOSFET2, and MOSFET3, the breakdown voltage is 588 V, 432 V, and 311 V, respectively. Due to the combination of different dielectric materials in the trench of MOSFET1 and MOSFET3, the modulation of electric field could be identified. As shown in Fig. 6, at points O_1 and O_2, two electric fields exist. The electric field distributions based on the analytical model described in Section 2 are in good agreement with the simulated results.

Table 2. Parameters of trench MOSFETs.

Symbol	Quantity	Value/μm
L	trench depth	16
W_t	trench width	4.8
W_{BOX}	BOX layer width	0.3
w_{11}	width of the left drift region	2
w_{12}	P-pillar width	0.5
w_{21}	width of the right drift region	1.5
w_{22}	N-pillar width	0.5
h	distance from point E to F	2

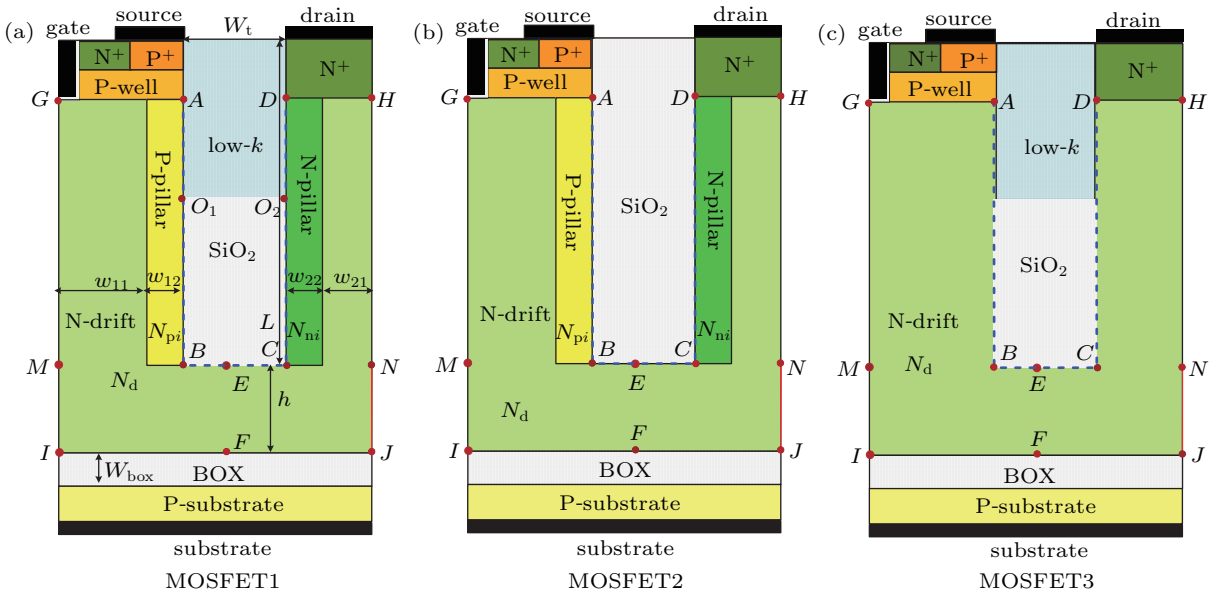


Fig. 5. Schematic diagram of (a) trench MOSFET1, (b) trench MOSFET2, and (c) trench MOSFET3.

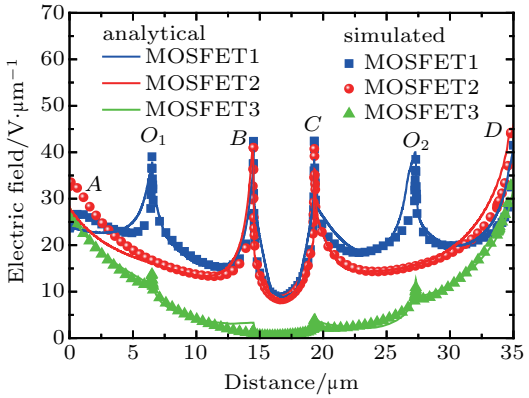


Fig. 6. The electric field distributions along A–O_1–B–C–O_2–D around the trench of the three types of the trench MOSFETs with the structure parameters as listed in Table 2. (The doping concentrations N_d, N_{pi} and N_{ni} of trench MOSFET1 are 4.5×10^{15} cm^{-3}, 3.3×10^{16} cm^{-3} and 5.0×10^{15} cm^{-3}, respectively. The doping concentration N_d of trench MOSFET2 and MOSFET3 is 4.3×10^{15} cm^{-3} and 3×10^{14} cm^{-3}, respectively. Breakdown voltage of the trench MOSFET1, MOSFET2, and MOSFET3 is 588 V, 432 V and 311 V, respectively.)

Figure 7 shows the symmetric distribution of electric field encircling the dielectric trench in trench MOSFET1. The analytical results of the electric field at various k_r are calculated by the conformal mapping. To achieve a symmetric distribution of the electric filed along the line A–B–C–D, three optimized parameters of $k_r = \varepsilon_k/\varepsilon_s = 1$, 1.8, and 2.5, and $N_d = 4.8\times10^{15}$ cm^{-3}, 4.7×10^{15} cm^{-3}, and 4.6×10^{15} cm^{-3} are given in Fig. 7. Under these parameters, as k_r increases, the doping concentration is reduced to keep a symmetric electric field distribution to realize higher breakdown voltage. Therefore, the analytical results of electric field are in a good agreement with the simulated results.

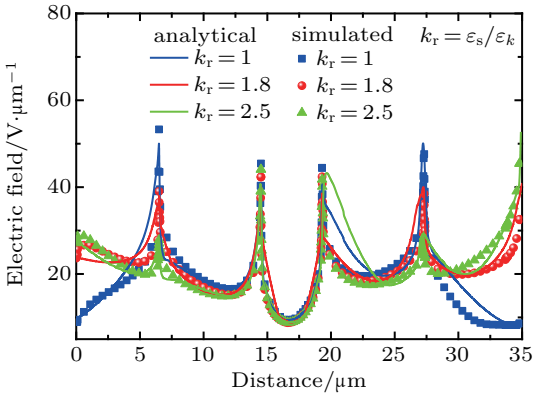


Fig. 7. The electric field distribution along A–B–C–D at low-k material in trench MOSFET1 with $k_r = 1$, 1.8, and 2.5. (The doping concentration of N/P pillar is $N_{pi} = 3.5\times10^{16}$ cm^{-3}, $N_{ni} = 5\times10^{15}$ cm^{-3}; the width of the dielectric trench is $W_t = 4.8$ μm, and the depth is $L = 4.8$ μm.)

In trench MOSFET1, the bias V_d of 577 V, 596 V, and 600 V is applied at drain–source at $N_d = 4.7\times10^{15}$ cm^{-3}, 4.5×10^{15} cm^{-3}, and 4.3×10^{15} cm^{-3}, respectively. The corresponding potential distributions of the four regions I, II, III, and IV around the trench along the line A–B–C–D are calculated by the potential model as aforementioned. As shown in Fig. 8, the slight variation of potential at point O_1 and O_2 is owing to the variation of k_r in the dielectric trench for introducing two electric field peaks, as shown in Figs. 6 and 7. The analytical potential distribution at point O_1 and O_2 also demonstrates the similar fluctuation. From point A to D around the dielectric trench with the potential distributions of $N_d = 4.3\times10^{15}$ cm^{-3} at $V_d = 577$ V, 4.5×10^{15} cm^{-3} at $V_d = 596$ V, and 4.7×10^{15} cm^{-3} at $V_d = 600$ V in trench MOSFET1 along A–B–C–D. Therefore, the analytical results exhibit good agreement with simulated results for the same conformity.

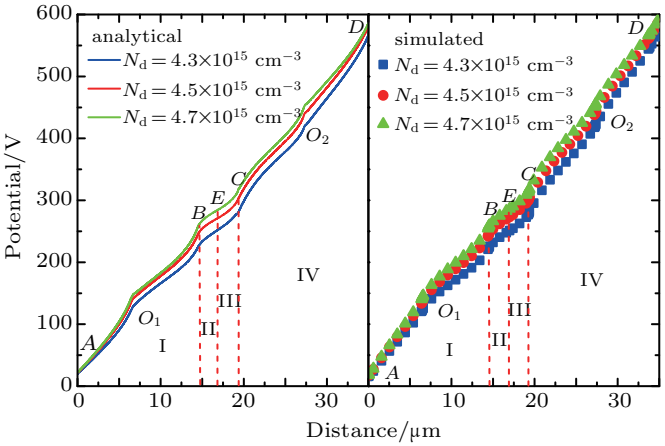


Fig. 8. The potential distribution of trench MOSFET1 with various doping concentrations for the drift region based on the analytical model and the simulation results.

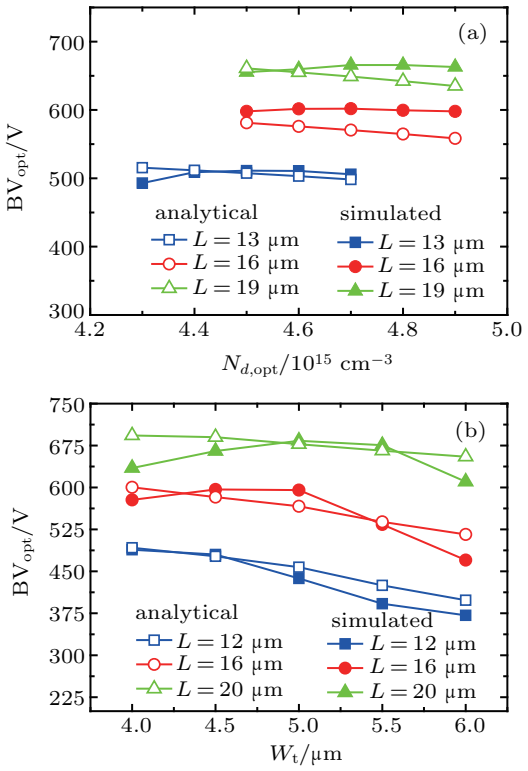


Fig. 9. Optimized BV_{opt} of trench MOSFET1: (a) optimized BV_{opt} versus doping concentration of drift region $N_{d,opt}$, and (b) optimized BV_{opt} versus trench width W_t.

Figure 9(a) shows BV_{opt} versus $N_{d,opt}$ in trench MOSFET1 at various depths of trench: $L = 13$ μm, 16 μm, and

19 μm. The larger depth L of trench can actually lengthen the folded drift region along A–O_1–B–C–O_2–D. It is found that as L increases from 13 μm to 19 μm, BV_{opt} increases from 497 V to 652 V. Due to the enhancement of dielectric electric field, the value of BV_{opt} can be kept at small fluctuation by the optimized $N_{d,opt}$. The optimized BV_{opt} versus W_t is also demonstrated in Fig. 9(b). In this case of $L = 16$ μm, the increase of W_t from 4 μm to 6 μm can also result in the BV_{opt} reduction from 577 V to 470 V. Meanwhile, the analytical BV_{opt} as given in Eq. (52) indicates the implicit relation of structure parameters. The analytical results are verified by the simulations in good agreement.

4. Conclusions

A dielectric trench is implanted in a power MOSFET to achieve a large drift region to enhance the breakdown voltage. The obtained dielectric trench filled with SiO_2 or low-k dielectric is compatible with the trench process. In this specific topology design of trench MOSFET, the conformal-mapping method is used to model the electric field distribution of the drift region. This conformal transformation allows us to analyze the electric field along the trench. Meanwhile, the approximated BV is also obtained to be dependent on the structure parameters, such as the dielectric permittivity for offering the design. The analytical results by conformal-mapping show good agreement with the simulations.

References

[1] Li P C, Luo X R, Luo Y C, Zhou K, Shi X L, Zhang Y H and Lv M S 2015 *Chin. Phys. B* **24** 047304
[2] Qiao M, Wang Y R, Zhou X, Jin F, Wang H H, Wang Z, Li Z J and Zhang B 2015 *Trans. Electron. Devices* **62** 2933
[3] Xia C, Cheng X H, Wang Z J, Cao D, Jia T T, Yu Y H and Shen D S 2013 *Trans. Electron. Devices* **60** 1279
[4] Zhou K, Luo X R, Xu Q, Li Z J and Zhang B 2014 *Trans. Electron. Devices* **61** 2466
[5] Hu S D, Zhang L, Luo J, Tan K Z, Chen W S, Gan P, Zhou X C and Zhu Z 2013 *Electron. Lett.* **49** 223
[6] Hu S D, Zhang L, Luo X R, Zhang B, Li Z J and Wu L J 2011 *Chin. Phys. Lett.* **28** 128503
[7] Luo Y C, Luo X R, Hu G Y, Fan Y H, Li P C, Wei J, Tan Q and Zhang B 2014 *Chin. Phys. B* **23** 077306
[8] Zheng Z, Li W and Li P 2013 *Chin. Phys. B* **22** 047701
[9] Luo X R, Yao G L, Zhang Z Y, Jiang Y H, Zhou K, Wang P, Wang Y G, Lei T F, Zhang Y X and Wei J 2012 *Chin. Phys. B* **21** 068501
[10] Zhou K, Luo X R, Fan Y H, Luo Y C, Hu X R and Zhang B 2013 *Chin. Phys. B* **22** 067306
[11] Shi X L, Luo X R, Wei J, Tan Q, Liu J P, Xu Q, Li P C, Tian R C and Ma D 2014 *Chin. Phys. B* **23** 127303
[12] Williams R K, Darwish M N, Blanchard R A, Siemieniec R, Rutter P and Yusuke Kawaguchi 2017 *Trans. Electron. Devices* **64** 674
[13] Luo X R, Zhang B, Li Z J, Guo Y F, Tang X W and Liu Y 2007 *IEEE Electron. Dev. Lett.* **28** 422
[14] Son W S, Sohn Y H and Choi S Y 2003 *Electron. Lett.* **39** 1760
[15] Wu L J, Zhang W T, Shi Q, Cai P F and He H C 2014 *Electron. Lett.* **50** 1982
[16] Yin C, Wei J, Zhou K and Luo X R 2015 *Electron. Lett.* **51** 1348
[17] Li W, Zheng Z, Wang Z G, Li P, Fu X J, He Z R, Liu F, Yang F, Xiang F and Liu L C 2012 *Chin. Phys. B* **21** 078502
[18] Zhao Y Y, Qiao M, Wang W B, Wang M and Zhang B 2012 *Chin. Phys. B* **21** 018501
[19] Udreaa F, Wang Y G, Deng H and Luo X R 2010 *Chin. Phys. B* **19** 077306
[20] Wei J, Luo X R, Zhang Y H, Li P C, Zhou K, Li Z J, Lei D M, He F Z and Zhang B 2015 *IEEE 27th Symposium on Power Semiconductor Devices and ICs*, May 10–14, 2015 Hong Kong, China, 15203419
[21] Hu X R and Lv R 2014 *Chin. Phys. B* **23** 128501
[22] Hu X R, Zhang B, Luo X R and Li Z J 2012 *Solid State Electronics.* **69** 89
[23] Hu X R, Zhang B, Luo X R, Wang Y G, Lei T F and Li Z J 2012 *Chin. Phys. B* **21** 078502
[24] Zhang Y H, Wei J, Yin C, Tan Q, Liu J P, Li P C and Luo X R 2016 *Chin. Phys. B* **25** 027306
[25] Huang J Q, He W W, Chen J, Luo J X, Lu K and Chai Z 2016 *Chin. Phys. Lett.* **33** 096101
[26] Jin Q X, Liu B, Liu Y, Wang W W, Wang H, Xu Z, Gao D, Wang Q, Xia Y Y, Song Z T and Feng S L 2016 *Chin. Phys. Lett.* **33** 098502
[27] Yuan S, Duan B X, Cao Z, Guo H J and Yang Y 2016 *Solid-State Electron.* **123** 6
[28] Wang B, Wang Z G and Sun J 2016 *IEEE International Conference on Solid-State and Integrated Circuit Technology*, October 25–28, 2016 Hangzhou, China, 17081943
[29] Wang Z G, Zhang B, Fu Q, Xie G and Li Z J 2012 *IEEE Electron. Dev. Lett.* **33** 703
[30] Wang Z G, Chen W J, Zhang B and Li Z J 2012 *Chin. Phys. B* **29** 107202
[31] Zeev N 1975 *Conformal Mapping* (New York: Dover Publications) pp. 266–332
[32] Panofsky W K H and Phillips M 1962 *Classical Electricity and Magnetism* (Reading: Addison-Wesley) pp. 245–363
[33] Chung S K 2000 *IEEE Trans. Electron. Dev.* **47** 1006